ERF2010_066

AERODYNAMIC AND AEROELASTIC ANALYSIS OF ROTORS AT HIGH ADVANCE RATIOS

Jean de Montaudouin Seun Do Heo Marilyn J. Smith Olivier A. Bauchau
jean3@mail.gatech.edu seun.heo@ae.gatech.edu ms55@mail.gatech.edu olivier.bauchau@ae.gatech.edu
Daniel Guggenheim School of Aerospace Engineering
Georgia Institute of Technology, Atlanta, Georgia, 30332-0150, USA

Abstract

The aerodynamic and aeroelastic behavior of a rotor become more complex as advance ratios increase to produce high speed forward flight. As the rotor blades encounter large regions of cross and reverse flows during each revolution, strong variations in the local Mach regime are encountered, inducing complex elastic blade deformations. In addition the wake system may remain in the vicinity of the rotor, adding complexity to the blade loading. The ability of current multi-body dynamics codes (CSD) using aerodynamics predicted with linear-based aerodynamic theory and more complex computational fluid dynamics (CFD) methods for rotors with advance ratios ranging from 0.5 to 2.0 is examined. Results indicate increasing vibratory loading at some high advance ratios may not be predicted with some lower-fidelity aerodynamic methods. This vibratory loading increases the sensitivity of the trim model, so that as advance ratio increases, the vibratory loading must in some cases be filtered to achieve a trim state. Trim to zero torque (an autorotative state) rather than a finite thrust target indicates that care must be taken with the CFD grid near the tip so that unphysical drag predictions not prevent a trimmed solution from being achieved.

NOMENCLATURE

c	rotor blade chord length, ft
C_D	drag coefficient
C_L	lift coefficient
M	Mach number
n	integer
N	number of rotor blades in a rotor
r	rotor radial location, ft
R	rotor tip radius, ft
T	time
u	generic output parameter
$\hat{y}$	generic target value
U	velocity, $\frac{ft}{sec}$
x, y, z	Cartesian streamwise,radial and normal lengths, ft
y^+	dimensionless wall spacing
α_{shaft}	shaft angle of attack, deg
μ	advance ratio, $\frac{U}{\Omega R}$
Ω	rotor angular velocity, RPM
ψ	azimuth location, deg
θ	collective angle, deg

INTRODUCTION

Conventional rotorcraft performance has been limited by attainable forward flight speeds. Significant efforts were expended to improve the design of conventional rotors during the 1960s and 1970s (e.g., Kisielowski at al. [1], Tanner [2], Sweet et al. [3], Ekquist [4], McCloud et al. [5], McHugh and Harris [6], Harris et al. [7], McCutcheon [8]) that increased the theoretical upper limit from 180 knots to 200-300 knots [6]. Alternatives to conventional helicopter designs, primarily tiltrotor and tiltwing compound options, have been also explored to increase rotorcraft forward flight limits, albeit with both cost and weight penalties.

An advance ratio of 0.5 (μ=0.5) is typically designated as the de facto upper limit of forward flight speed of single rotor helicopters based on the impact of retreating blade stall on the lift and propulsive force. In the past decade, the slowed rotor concept has garnered interest. In this approach rotors attain much higher advance ratios yet minimize the drag arising from the transonic Mach regime on the advancing side of the rotor disk. However, as the rotor sweeps from the advancing to the retreating side (and vice versa), the rotor experiences edgewise velocities along the radius that are comparable to the velocities in the chordwise direction as well as large areas of reverse flow [9]. This rapidly changing velocity field can induce elastic deformations that are very large and may cause rotor instability that until recently could not be efficiently controlled. New technological advances however, have allowed the slowed rotor concept to be successfully demonstrated for advance ratios that exceed 1.0 [10].

The potential for achieving these high flight speeds in single rotor helicopters is attractive, but as Johnson [11] noted in 2008, existing analysis tools and databases of aerodynamic information either are or may be inadequate to support the design and analysis of advanced concepts. There are two fundamental types of aeroelastic simulations in use today for rotorcraft design and analysis: comprehensive methods and Reynolds-Averaged Navier-Stokes (RANS) CFD-CSD coupling. Comprehensive codes [12–16] have been developed to provide airloads trends for rapid turnaround needed for design and for industry applications, and they are currently characterized by the utilization of finite-element structural methods combined with lower-fidelity aerodynamics, such as lifting-line, dynamic inflow, and prescribed or free wake models. CFD-CSD coupling methods [such as Refs. 18–21] provide the higher fidelity aeroelastic analysis of a rotor as they can more accurately capture viscous and vorticity influences on the rotor, but at much higher computational costs and time.

This effort explores the ability of comprehensive code and CFD-CSD coupling to predict the elastic behavior of a model rotor at advance ratios of 0.5 and higher, and include correlation to recent tests [22–24]. The results of the two different methods are compared, and discussions concerning the ability and robustness of these methods when applied to configurations at high advance ratios are presented.

MODEL-SCALED TEST ROTOR

A model rotor was built and tested by Continuum Dynamics, Inc. [22–24] at the Glenn L. Martin Wind Tunnel at the University of Maryland for increasing advance ratios from approximately 0.5 to 2.0. The model rotor, schematically represented in Fig. 1, consisted of three rotor blades with a radius of 22 inches, offset from the hub by 4 inches. Each rotor blade was a rectangular, untwisted planform constructed from a NACA0012 airfoil. The rotor was fully articulated and a concentrated mass was located at 80% of the span from the blade root. The influence of the model support structure in the wind tunnel was not modeled, and the model blockage was determined to have minimal impact on the results, so that the wind tunnel walls were not included in the computations.

A sweep of advance ratios from the test results reported by Quackenbush et al. [24] were utilized for correlation with the CFD-CSD analyses. This set of data, denoted as Run 6 in Ref. [24] and Table1 consisted of a campaign at a free-stream velocity of 115 fps where, the shaft angle of attack was decreased from 4.8°to 0.8°, by increments of 0.7 to 0.25°. For each of these configurations, the rotor speed, lift coefficient, drag coefficient, and mean collective setting that corresponded to autorotation were measured.

Table 1: Experimental data (Run 6) [Ref. 24]

α_{shaft} (°)	Ω RPM	Mu	C_L $\times 10^{-2}$	C_D $\times 10^{-3}$	θ (°)
4.8	975	0.5420	3.4912	9.8672	-0.2014
4.3	870	0.6073	2.9205	8.2415	-0.2955
3.8	750	0.7046	2.373	6.7182	-0.5137
3.4	680	0.7771	2.0765	5.7835	-0.6136
3.0	560	0.9436	1.7875	4.7192	-0.8076
2.7	515	1.0262	1.7002	4.2981	-0.9075
2.2	420	1.2583	1.5527	3.5666	-1.0781
1.9	360	1.468	1.4641	2.9134	-1.1313
1.65	315	1.677	1.3081	2.551	-1.1179
1.4	290	1.8223	0.1100	2.1887	-1.1048
1.1	275	1.9217	0.0942	1.8768	-1.0059
0.8	260	2.0326	0.0712	1.5035	-0.9338

COMPUTATIONAL STRUCTURAL DYNAMICS MODELING

The computational structural dynamics modeling was accomplished using the multi-body code, DYMORE, developed at Georgia Tech by Bauchau [15]. DYMORE uses geometrically exact nonlinear beam elements to model the elastic blade, and a library of methods to model multi-body components.

Figure 2 illustrates the model of the three-bladed rotor system that was numerically investigated. The rotor hub is clamped at an inertial point by means of a shaft with stiffness properties much higher than those of the blades. The shaft has a length of 2.4 in. The angular velocity of the hub is prescribed to a constant value, Ω, by means of a revolute joint. Flap and lag hinges are used to connect the hub to the three blades. The flap and lag hinges are located at 2.25 in and 4 in from the shaft, respectively. Very soft springs and dampers were present in the flap hinge to avoid singularities in the model; the spring constant was 1×10^{-4} ft.lbs/rad and the dashpot constant is 1×10^{-4} ft.lbs.sec/rad. A similar arrangement was used for the lag hinge. The same spring of stiffness constant as the flap hinge was used and the dashpot constant was selected to be 2×10^{-1} ft.lbs.sec/rad to reflect dry friction in the screw attachment at the blade's grip.

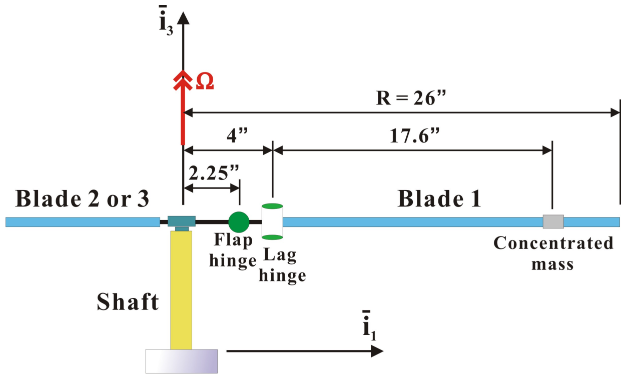

Figure 1: Rotor test configuration

Each blade featured a concentrated mass located at 80% of the span from the blade root. For the finite-element analysis, each blade was modeled with nine cubic elements. The blade had a length of 22 in, and the rotor radius was 26 in. The blade collective pitch was set at +1°. Gravity loading was also considered in the model. The rotor remained in the horizontal plane, and the gravity vector was inclined about axis by an $\alpha_{shaft}$to reflect the tilting of the shaft.

For the aerodynamic model, simplified airloads were computed using a table look-up procedure. The far field free stream flow velocity was kept constant at 110 ft/sec. The flow vector was inclined to reflect the tilting of the α_{shaft}. Standard air properties were used, and the NACA 0012 airfoil tables were used for the simulation. The Peters unsteady aerodynamics and the dynamic inflow models [26] were used to capture the effects of unsteady inflow field. Aerodynamic loads were computed at 12 airstations along the span of the blade. A tip loss factor of 0.95 was included in the model.

Trimming for the CSD and CFD-CSD simulations was achieved via a quasi-steady trimmer within DYMORE. This trimmer is based on a control law designed to determine the outputs $\underline{u}$ that will drive the system to a configuration where the input match the specified target values $\hat{\underline{y}}^T = \lfloor \hat{y}_1, \hat{y}_2, \ldots, \hat{y}_N \rfloor$. It modifies the controls proportionally to the output error so as to drive the inputs to their target values. This is done through two phases: the *Reference phase* and the *Adjustment phase*, with two corresponding user-defined time spans as follows T_{ref} time span will be taken to establish the *reference configuration* of the system for the reference output values $\bar{\underline{u}}$. At the end of the reference run, the input values are denoted $\bar{\underline{y}}$. It is important to simulate the response of the system for a period that is long enough to allow the dynamics of the system to settle, *i.e.*, for $\bar{\underline{y}}$ to settle to steady values.

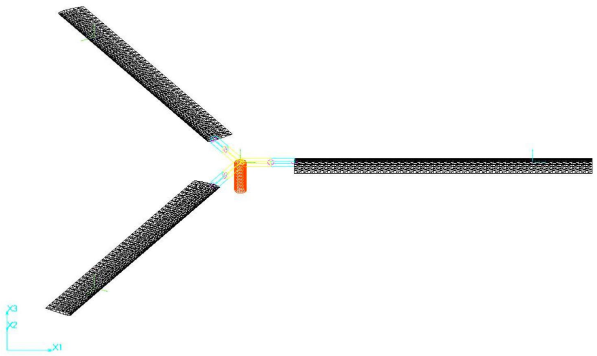

Figure 2: Multibody simulation model of the test rotor.

Computational Fluid Dynamics Modeling

The computational fluid dynamics equations were resolved using the structured mesh methodology, OVERFLOW [27]. OVERFLOW provides a plethora of options for the solution of the compressible RANS equations, and has been used extensively for rotorcraft applications, including CFD-CSD loose coupling (for example, Refs. [18, 19]. Spatial algorithms vary from 2^{nd}-order central difference schemes to 6^{th}-order WENO schemes. Time accuracy is achieved via second-order dual time stepping or Newton subiterations. Turbulence simulation options include a large selection of RANS, hybrid RANS-LES, and LES/VLES methods.

For the dynamic rotor blade simulations in this effort, the time step was set to provide 7200 iterations per revolution. This time step was applied with an ARC3D diagonalized Beam-Warming scalar pentadiagonal scheme and 2^{nd}-order accurate Newton sub-iterations for the temporal integration. A 4^{th}-order spatial discretization formulation was employed with central difference Euler terms and a spectral radius dissipation scheme.

The computational grids consisted of six grids on each rotor blade (Fig. 3). Three of the grids model the blade as the blade is divided between into the root, the main body and the tip. The other three grids consist respectively of the root and tip end caps and a local rectangular background grid whose purpose is to reduce errors during hole cutting. The main rotor blade grid is an O-H grid with 299 nodes around the rotor airfoil, 113 nodes along the rotor radius, and 82 nodes normal to the surface. The initial normal spacing at the surface was set so that the y+ < 1 to ensure sufficient grid points within the boundary layer. The end caps to model the root and tip sections of the rotor blade included 91 meridian points, 69 longitudinal points, and 60 normal points. The three rotor blades were situated to model the test rotor of Fig. 1 with a background grid consisting of outer boundary cell size of 0.25 chord width and cells near the rotor of 0.07 chord or less.

A loose coupling strategy is used to exchange data between the CFD and CSD codes at regular intervals, typically a full revolution of the rotor or a multiple of the fraction $1/3$ $(1/N)$ thereof. The "delta airloads approach" [18] has been widely used by many researchers to obtained trimmed solution for rotorcraft in forward flight. This computationally efficient approach yields a trimmed, periodic solution of the problem.

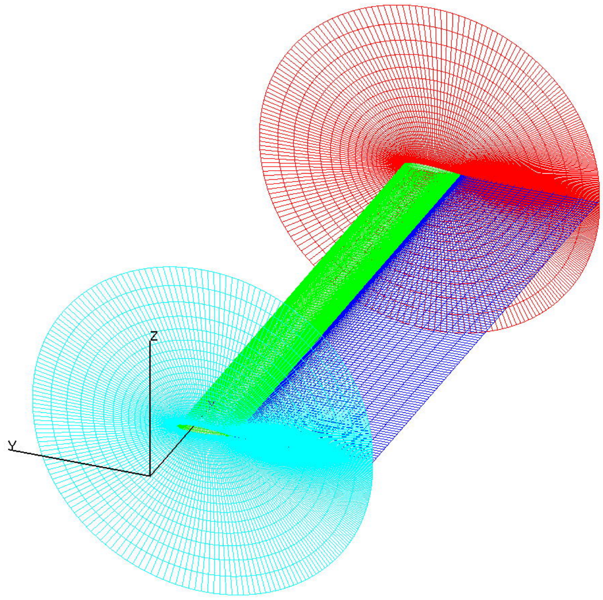

Figure 3: Computational grids about the rotor blade

Determination of Autorotation for the Three-Bladed Rotor

The experimental campaign was performed by setting the tunnel speed and slowing the rotor down until autorotation occurred. Thus, the ability of the CSD code to be able to trim and correctly predict at minimum the characteristic trend of the data was evaluated. To explore this, for each equilibrium case of experiment where the wind velocity impinges on the upper side of the rotor blade (downward wind), given the shaft angle, two numerical simulations were performed at two different rotor speeds, located near the experimentally measured equilibrium rotor speed. The zero torque condition was then estimated by linear interpolation between these two results. This interpolated rotor speed at zero torque is referred to as the "torque-free rotor speed", and the thrust at the same speed the "torque-free thrust". Table 2 lists the torque-free rotor speeds of both experiment measurements and numerical predictions, together with the relative differences. In all cases the CSD method was able to predict a torque-free rotor speed with 30–40 rpm of experiment. This yielded small errors at the highest shaft angles, although the relative error tends to increase for lower values of the shaft tilt angle where the rotor speed was also decreasing.

Applying this process, torque-free rotor speeds were computed and are shown Figs. 4 and 5. Figure 4 includes both experiment measurements and numerical predictions, together with the relative differences. In all cases a good agreement is observed, although the discrepancy tends to increase for lower values of the shaft tilt angle. Figure 5 illustrates the predicted thrust as a function of shaft tilt angle.

A second set of simulations was evaluated for upward wind directions. The directions of far field flow velocity and gravity vector were inclined by α_{shaft}such that the wind was upward to the rotor disk, impinging on the lower surface of the rotor blade. In the upward wind case, it was not possible to find an autorotation condition. A second set of simulations was run for the upward wind directions. Seven shaft tilt angles, α_{shaft}, tested experimentally were simulated using the experimentally measured rotor speed in each case. Figure 6 depicts the change in thrust and torque as a function of shaft tilt angle.

Table 2: Torque-free rotor speed comparisons

α_{shaft} (deg.)	Torque-free rotor speed (rpm)		Relative difference (%)
	Experiment	Prediction	
5.0	1005	1007.20	0.22
4.4	830	885.15	6.64
3.8	720	764.69	6.21
3.2	575	618.48	7.56
2.55	420	475.72	13.27
2.2	365	399.00	9.32
2.0	282	332.41	17.88

HIGH-FIDELITY AEROELASTIC SIMULATIONS

CFD-CSD loose coupling simulations were performed for a subset of the experimental data (Run 6) (Table 1) obtained in the experimental campaign described in Quackenbush [24]. These data included advance ratios ranging from 0.5 to 2.0, and were again obtained at autorotation conditions within the tunnel. As noted in the prior discussion, it was possible to obtain the autorotation location via an iterative process within DYMORE. Given the cost in iterating to determine the autorotation conditions with CFD-CSD coupling, two alternative trim schemes were employed with a predetermined rotor speed. The first method employed trimming to the experimental thrust coefficient, which is typically the method employed by most loose coupling approaches. The second approach was to trim as close as possible to a zero torque condition.

Three advance ratios, 0.54, 1.0, and 1.5 were evaluated with CFD-CSD coupling. The process involved an initial iteration of the CFD solver for an entire rotor revolution using elastic deflections and a trim obtained from the CSD case alone. This permitted the initial CFD starting transients to settle to a near-periodic solution.The rotor speed observed in the experiment (Table 1) was assumed to be close to the autorotation speed, based on the prior autorotation assessment with DYMORE. There are two ways to perform the loose coupling at this juncture. One method updates the CFD-CSD coupling at each $1/N$ revolution, where N is the number of rotor blades, where in this instance, N=3. The other method allows the CFD code to obtain a near-periodic response to the new controls and blade motions by running for some n/N revolutions, where n is dependent upon the actual rotor response, and then performs the coupling. For the advance ratios lower than $\mu = 0.54$, the loose coupling process did not encounter any issues in numerical stability using the $1/N$ coupling update approach. At higher μ values (0.5 and above), however, the first 1–2 coupling iterations encountered fewer trim numerical stability issues if the n/N approach was employed. For these simulations, a $n = 2$ was sufficient to reach periodicity. By the third or fourth coupling iteration (iteration = 2 or 3), a $1/N$ CFD revolution was sufficient to maintain avoid numerical instabilities during trim.

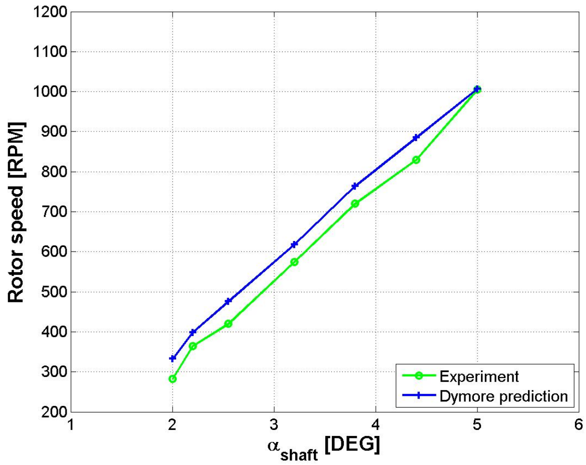

Figure 4: Torque-free rotor speed comparison.

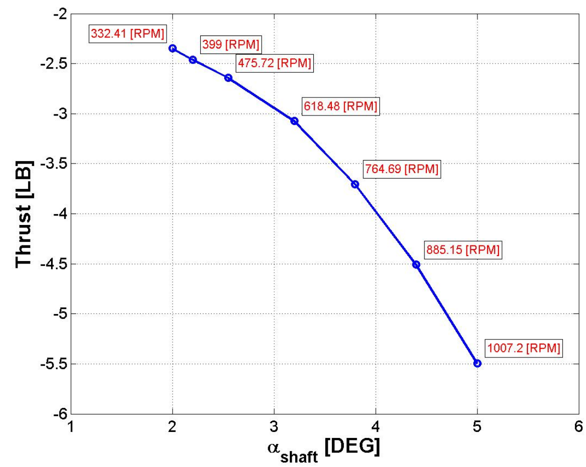

Figure 5: Torque-free thrust vs. α_{shaft}.

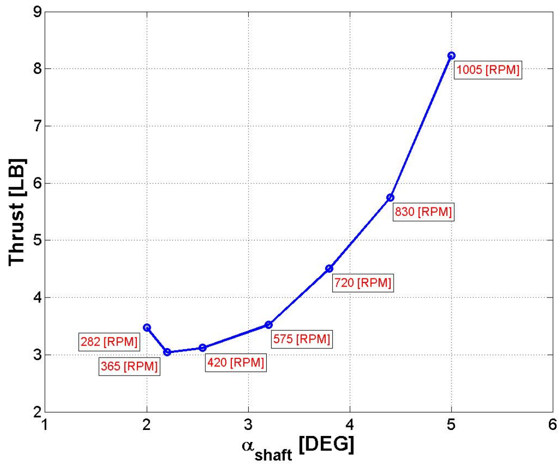

(a) Thrust

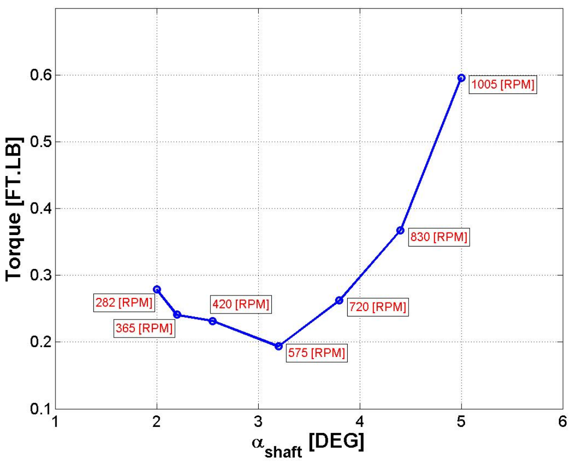

(b) Torque

Figure 6: Thrust and torque as a function of α_{shaft}tilt angle for the upward wind direction.

Some additional numerical stability issues were encountered for these high advance ratios. The slowed rotor with increased free stream flow resulted in a very different vortex wake pattern encountered by the rotors on the aft portion of the disk, as illustrated in Fig. 8. At the lowest advance ratio, μ = 0.54, the tip vortex of blade 1 curves around and encounters the next blade on the upper surface in the fourth (aft rotor disk, retreating side) and first rotor quadrants (aft rotor disk, advancing side). The root vortex from blade 3 also contributes some minor parallel blade vortex interaction on blade 1. This results in moderate torsional response of the blade (Fig.9a, right) between ψ = 330°to 45°. As expected, this torsional response is not observed for the CSD prediction using the dynamic inflow model (Fig.9a, left figure).

When the advance ratio is increased to μ = 1.0, the vortex-blade interaction becomes much more significant, as observed in Fig. 8b. Here, the vortex strength has dramatically increased (q-criterion is an order of magnitude higher), and the strong tip vortex from blade 3 creates a parallel vortex interaction over almost the entire radius of blade 1. Note that there are two tip vortices emanating in this figure from blade 3, which appear to be the result of the large cross-flow at this azimuthal location so that the leading and trailing edge of the blade 3 tip act as "wing tips" in a streamwise flow. These vortices further interact with the root vortices from blades 3 and 1, generating strong pressure fluctuations in the fourth rotor quadrant. The impact of the shed wake is immediately discernible during the CFD-CSD coupling process through primarily the torsional response of the system, illustrated in the right figure of Fig.9b. A high frequency vibration is observed over the rotor disk, with strong responses present in the fourth quadrant. On the advancing side, these torsional responses are relatively small (within ±0.5°), but increase on the retreating side to 9°excursions (-6°to 3°). The CSD response prediction using finite-state theory (Fig.9b, left figure) does not resemble the coupled solution as it does not have the capability of predicting this vibratory response.

As the advance ratio increases further to μ = 1.5, the rotor blade-wake interaction becomes less severe, as illustrated in Fig. 8c. The increased free stream velocity now translates the strong blade 3 tip wakes outboard so that they miss all but the tip of blade 1 at the 0°azimuth location. In addition, the orientation of the tip vortices in the fourth quadrant results in blade-vortex interactions that are no longer primarily parallel. The corresponding response to this alleviation of blade-vortex interactions are seen in Fig.9c (right picture). There is a 1/rev response in torsion to the rapidly expanding reverse and cross flow regions on the retreating side of the rotor. The torsional response is again similar to that of the CSD method using lower-fidelity aerodynamics (finite state theory), indicating that the response is primarily due to linear aerodynamics and not nonlinear blade-vortex interaction.

The loose-coupling process, as noted earlier, had some difficulty in attaining trim with the CSD methodology for the higher advance ratios, in particular, μ=1.0 (Fig.7). With the combination of the n/N and $1/N$ coupling updates, after 7 coupling iterations and 4 revolutions, the simulation had still not converged (in contrast to 3–4 coupling iterations for μ=0.54). By manual adjustment of the collective, the simulation converged within 2 coupling iterations (2/3 revolution). Using the thrust as a guide, convergence at each of the advance ratios has been characterized as a damping ratio, as shown in Table 3. Lower advance ratios, such as μ=0.54 and below converge rapidly (within 3-4 iterations using the n/N approach). The μ=1.0 case however has great difficulty in achieving convergence due to the high harmonic content. Indeed, the original loading from the CFD code caused numerical instabilities when attempting to trim due to very high harmonic content. This required the use of a Fast-Fourier Transform (FFT) on the loads and moments to filter out harmonic content greater than 21–22. For higher advance ratios, the convergence rate improves, but does not attain the rapid convergence observed for the advance ratios below one. Another measure of the convergence is the amount that the trim parameter deviates from its eventual mean. This trend is similar to that of the damping ratio, in that the advance ratio that has the most problem attaining trim (μ= 1.0) encounters much larger deviations at each coupling iteration, in some cases by an order of magnitude compared to the other two advance ratios studied. This does not appear to be driving the slow convergence rate, but may be an artifact of the complex nonlinear loading that the delta airloads protocol must resolve.

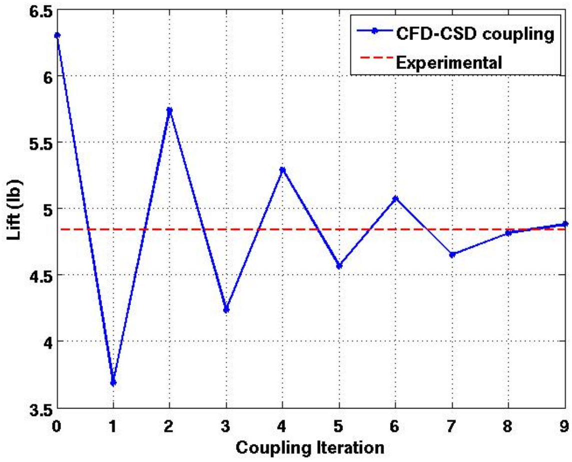

Figure 7: Thrust convergence at μ = 1.0.

Table 3: Evaluation of trim numerical stability

Advance ratio	Damping ratio
0.54	2.2
1.0	0.27
1.5	0.75

Independent of these numerical stability considerations, the second approach consisting of trimming as close as possible to a zero-torque condition proved to be problematic. This was not only a consequence that torque is highly dependent of the drag, which is subject to larger numerical error than lift. The difficulties encountered during trim were mainly due to the force prediction at blade tips. In many structured methods, such as the one applied in this effort, overset grids provide wing-caps used to model the rotor blade root and tip geometry. As the advance ratio was increased, non-physically large viscous forces were observed in these areas. This force increase within the tip cap area is not isolated to this study, but has been observed with other structured Navier-Stokes simulations [25]. At lower advance ratios and when trimming to thrust, this phenomenon has not been observed to be significant. When attempting to trim to autorotation, these forces can prevent success with these non-physically large values. To nullify these non-physicaly tip forces, the blade grids can be further refined so that these forces do not develop during the CFD simulation. An alternate approach is to neglect the pressures over the last 0.5–1% of the blade radius when integrating the equivalent airloads for the CSD lifting line.

The collective angle for the CFD-CSD and CSD methods are compared with experimental values (Fig. 10). The trend of collective angle to achieve trim using thrust coefficient predicted by the CSD method was similar to the trend for the CFD-CSD coupling. When the CFD-CSD coupling simulations were trimmed to zero torque using a fixed rotor velocity (from experiment) a trend similar of the experimental data autorotation collective is obtained. There is an offset between the experiment and CFD-CSD coupled predictions that may be a result of not changing the rotor speed during the simulations. It should be noted also that Quackenbush [23] observed that the collective measurement was difficult to obtain during the experimental campaign and may be subject to some errors.

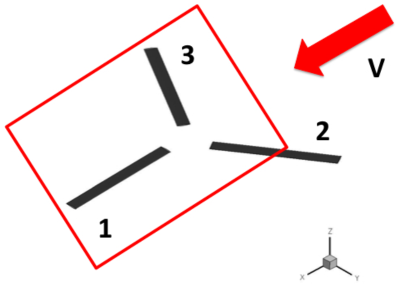

Figure orientation

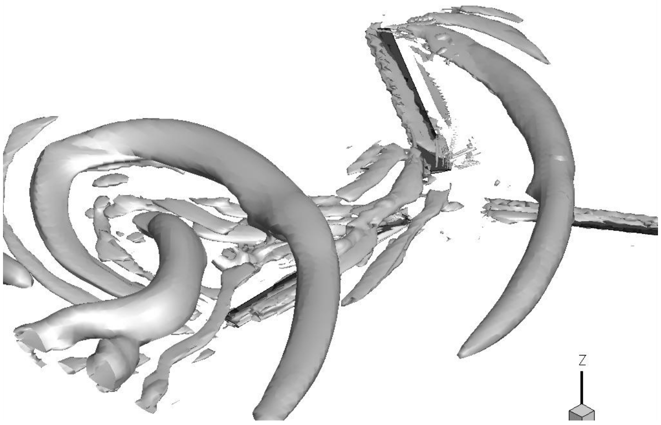

a) μ = 0.5

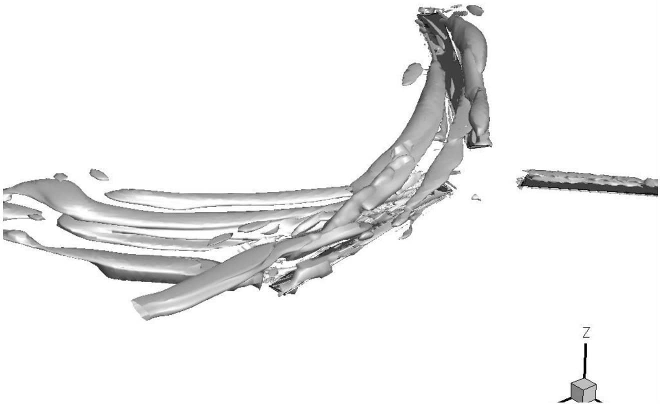

b) μ = 1.0

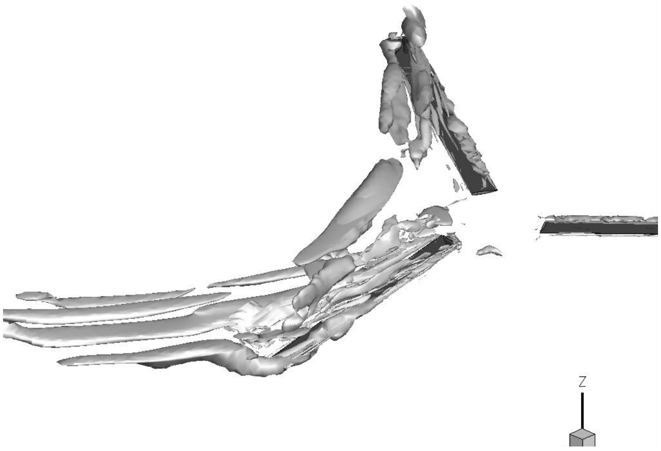

c) μ = 1.5

Figure 8: Contrast of shed wake patterns at different advance ratios. Q-criterion values are increased with increasing advance ratio to provide a clear visual perspective of the wake.

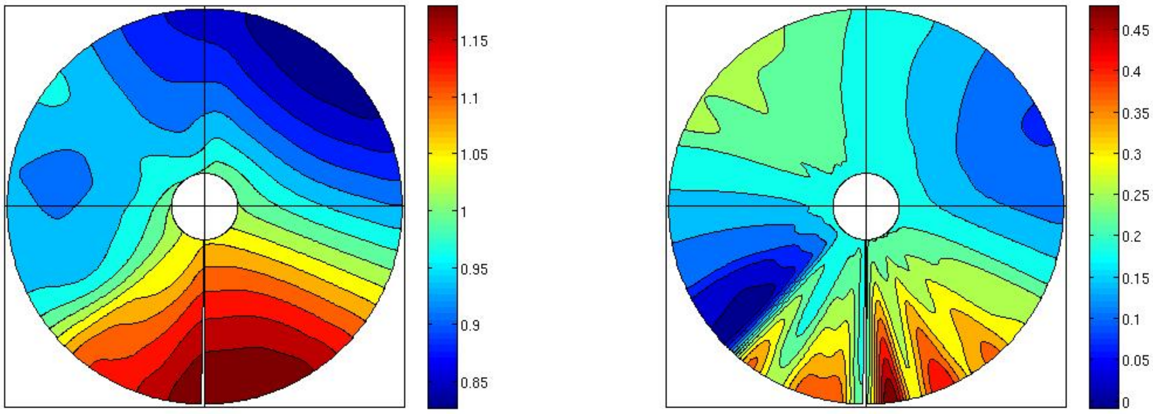

a) μ = 0.5

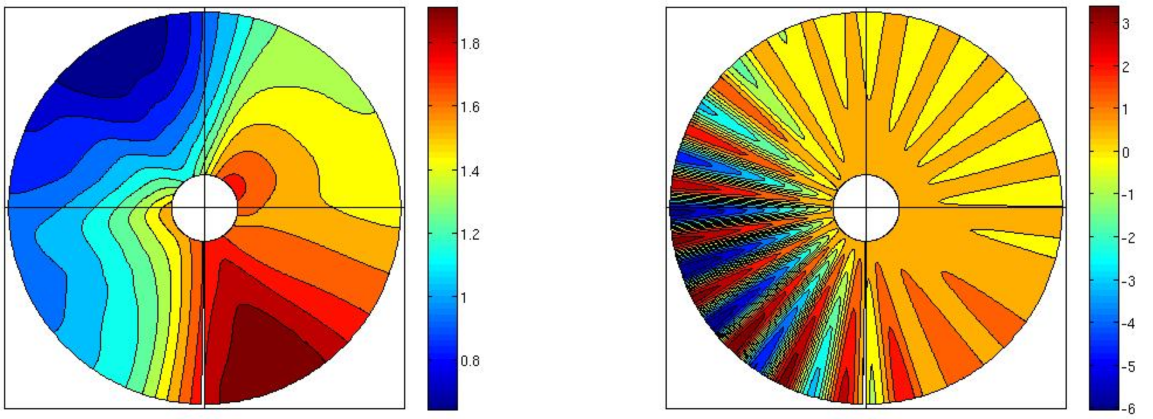

b) μ = 1.0

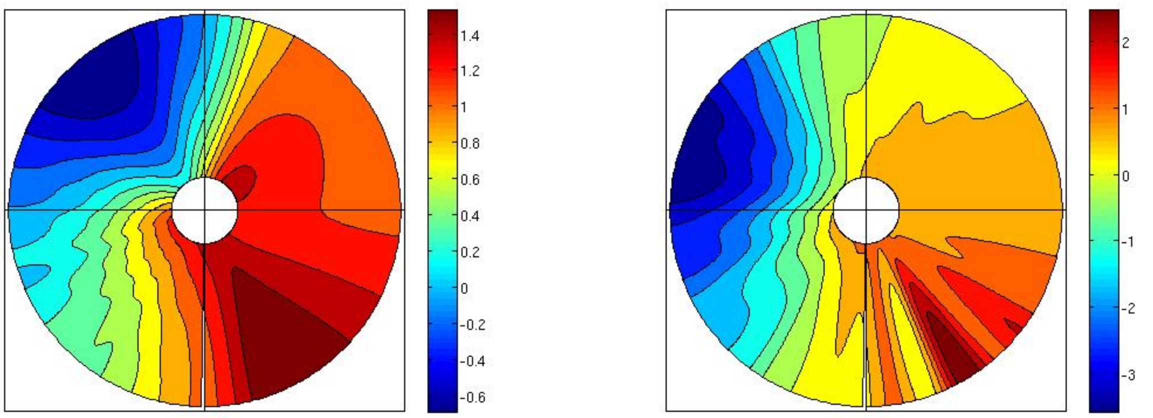

c) μ = 1.5

Figure 9: Comparison of the pitching response (deg.) at different advance ratios. The motion on the left column is CSD-alone (DYMORE) and the right column is CFD-CSD coupling. Note that due to the change in the behavior of the rotor, in order to illustrate the motion, the contour levels are not identical.

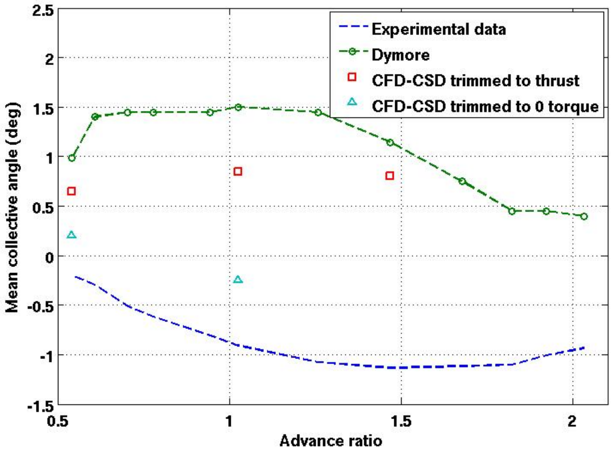

Figure 10: Collective angle changes with advance ratio.

The normal forces and pitching moments for the CFD-CSD coupling at the different advance ratios are shown in Fig. 11. As advance ratio increases, the forward side of the disk for the normal forces show overall the same trend, with the exception of azimuths beyond approximately 120°. The aft portion of the rotors are striking different due to the influence of the pitching or torsional response, in particular for μ=0.5. The pitching moments increase on the retreating rotor with advance ratio, and the largest pitching moments shift forward with the expansion of the reverse flow region with advance ratio.

CONCLUSIONS

Current numerical methods applied to rotors have been tested and compared to a model rotor for advance ratios greater than 0.5, characteristic of slowed rotor configurations. The CSD methodology applied both finite-state theory and CFD (CFD-CSD loose coupling) to obtain blade airloads. The following observations can be made for these processes:

- CSD methods can predict the trends of rotor rotational velocity necessary to achieve autorotation at given collective and shaft angle.
- CSD methods will require at minimum a free-wake methodology or CFD to capture the nonlinear behavior of the rotor at advance ratios of approximately one or higher due to the complex blade-wake interaction.
- Numerical instabilities may occur in the trimming process used in CFD-CSD loose coupling via the delta airloads method because of high harmonic content from vibratory loading. A Fast Fourier Transform with a low-pass filter to nullify these high vibratory loads (harmonics above 21-22) may be necessary.
- The $1/N$ loose coupling protocol may pass transients to the CSD trim module during the initial coupling iterations. A n/N loose coupling protocol is recommended for the first 2–3 coupling iterations.
- High vibratory loading at an advance ratio of one, and possibly other advance ratios, can cause the cost of CFD–CSD coupling to increase substantially.

ACKNOWLEDGMENTS

This work was supported via a NASA/Ames SBIR Phase II effort entitled "Next Generation Modeling Technology for High Speed Rotorcraft". The technical monitor is Dr. William Warmbrodt. The authors would like to thank Dr. Todd Quackenbush at Continuum Dynamics, Inc. for technical discussions and data from the experimental campaigns referenced within this paper.

References

[1] Kisielowski, E., Bumstead, R., Fissel, P., Chinsky, I., and DIV, B., "Generalized Rotor Performance," U.S. Army Aviation Material Laboratories Technical Report 66–83, AD 648874, 1966.

[2] Tanner, W., "Charts for Estimating Rotary Wing Performance in Hover and at High Forward Speeds," NASA CR–114, 1964.

[3] Sweet, G., Jenkins, J. L., and Winston, M. M., "Wind-Tunnel Measurements on a Lifting Rotor at High Thrust Coefficients and High Tip-Speed Ratios," NASA TN D–2462, 1964.

[4] Ekquist, D., "Design and Wind Tunnel Test of a Model Helicopter Rotor Having an Independently Moveable Inboard Blade Panel," Boeing Co., Morton PA, Vertol Div., 1965.

[5] McCloud, J., Biggers, J., and Stroub, R., "An Investigation of Full-Scale Helicopter Rotors at High Advance Ratios and Advancing Tip Mach Numbers," NASA TN D-4632, 1968.

[6] McHugh, F. J. and Harris, F. D., "Have We Overlooked the Full Potential of the Conventional Rotor" *Proceedings of the American Helicopter Society 31st Annual Forum*, May 1975.

[7] Harris, F., Tarzanin Jr, F., and Fisher Jr, R., "Rotor High Speed Performance, Theory vs. Test," *Journal of the American Helicopter Society*, Vol. 15, No. 3, 1970, pp. 35–41.

[8] McCutcheon, R., "S–67 Flight Test Program," *Proceedings of the 28th American Helicopter Society Annual Forum*, Vol. 28, 1972.

[9] Sissingh, G., "Dynamics of Rotors Operating at High Advance Ratios," *Journal of the American Helicopter Society*, Vol. 13, No. 3, 1968, pp. 56–63.

[10] Carter, J., "Extreme mu rotor," 2006, US Patent 6,986,642.

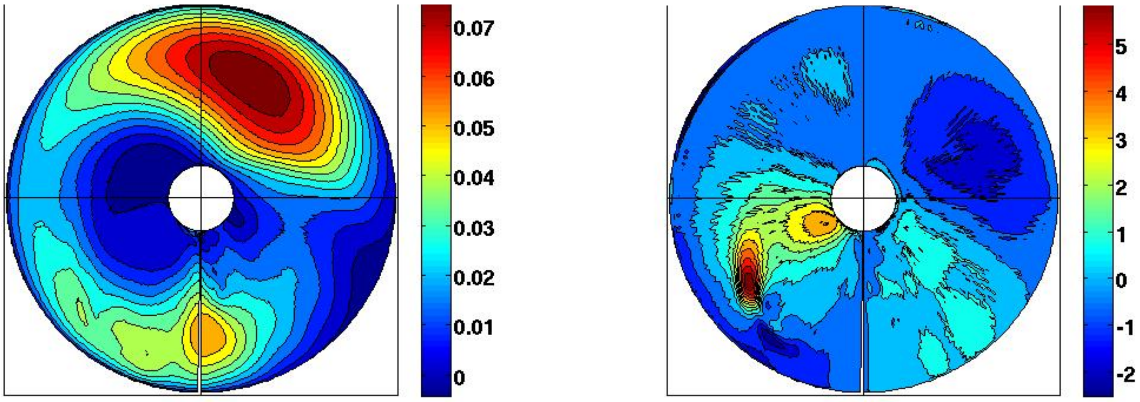

a) $\mu = 0.5$

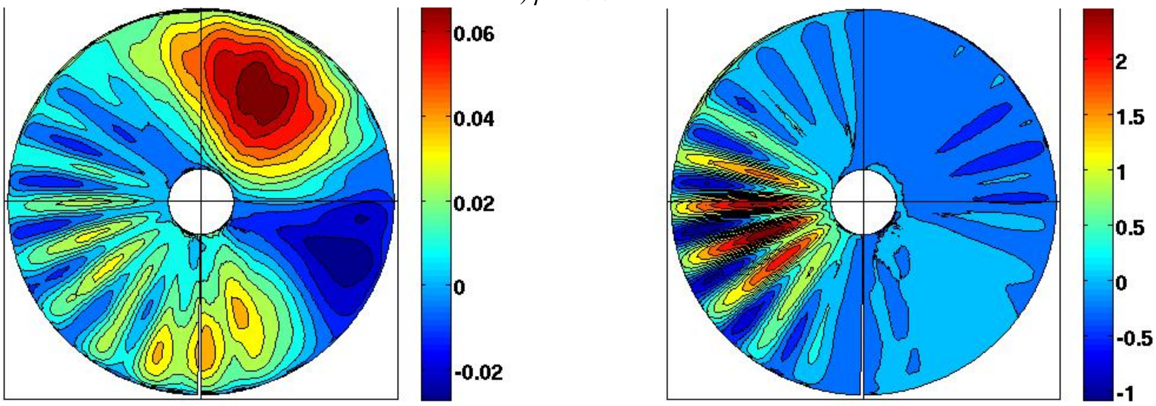

b) $\mu = 1.0$

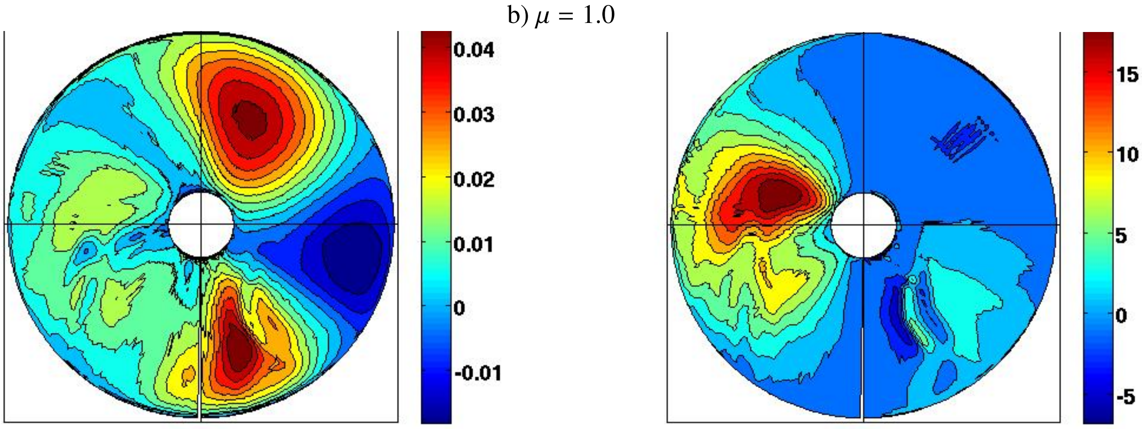

c) $\mu = 1.5$

Figure 11: Comparison of the normal force (lbs.) and pitching moments (ft.lbs.) at different advance ratios. Normal forces are presented as figures in the left column; pitching moments are shown in the figures to the right.

[11] Johnson, W., "Requirements for Next Generation Comprehensive Analysis of Rotorcraft," *Proceedings of the AHS Aeromechanics Specialists' Conference*, San Francisco, CA January 23–25, 2008.

[12] Johnson, W., "Rotorcraft Dynamics Models for a Comprehensive Analysis," *Proceedings of the 54th American Helicopter Society Annual Forum*, Washington D.C., May, 1998.

[13] Sopher, R. and Hallock, D., "Time-History Analysis for Rotorcraft Dynamics Based on a Component Approach," 2nd Decennial Specialists' Meeting on Rotorcraft Dynamics, Moffett Field, CA, November, 1984.

[14] Benoit, B. , Dequin, A. M., Kampa, K., Grunhagen, W., Basset, P.-M., and Gimonet, B., "HOST: A General Helicopter Simulation Tool For Germany and France," *Proceedings of the 56th American Helicopter Society Annual Forum*, Virginia Beach, VA, May, 2000.

[15] Bauchau, O. A., Bottasso, C. L. and Nikishkov, Y. G., "Modeling Rotorcraft Dynamics with Finite Element Multibody Procedures," *Mathematical and Computer Modeling*, 33, pp. 1113-1137, 2001.

[16] Wachspress, D.A., et al. "First-Principles, Free-Vortex Wake Model for Helicopters and Tiltrotors," AHS 59th Ann. Forum, Phoenix, AZ, 2003.

[17] Abras, J. N., *Enhancement of Aeroelastic Rotor Airload Prediction Methods*, PhD Dissertation, Georgia Institute of Technology, Advisor: Prof. M. J. Smith, March 2009.

[18] Potsdam,M., Yeo, H., and Johnson,W., "Rotor Airloads Prediction Using Loose Aerodynamic/Structural Coupling," *Journal of Aircraft*, Vol. 43, No. 3, May-June 2006.

[19] Shelton, A. B., Braman, K., Smith, M. J., and Menon, S., "Improved Turbulence Modeling for Rotorcraft," 62nd American Helicopter Society Annual Forum, Phoenix, AZ, May, 2006.

[20] Abras, J. and Smith, M. J., "Rotorcraft Simulations Using Unstructured CFD-CSD Coupling." *Proceedings of the AHS Specialists Meeting*, San Francisco, CA, January 2008.

[21] Beaumier, P., Costes, M., Rodriquez, B, Poinot, M., Cantaloube, B., "Weak and Strong Coupling Between the elsA CFD Solver and the HOST Helicopter Comprehensive Analysis," *Proceedings of the 31st European Rotorcraft Forum*, Florence, Italy, September 13–15, 2005.

[22] Quackenbush, T.R., and Wachspress, D.A., "Measurement and Analysis of High Advance Ratio Rotor Performance," *Proceedings of the* 64th *Annual Forum of the American Helicopter Society*, Montreal, Canada April 29–May 1, 2008.

[23] Quackenbush, T.R., Wachspress, D.A., McKillip, R. M. (Jr), and Sibilia, M. J., "Experimental and Analytical Studies of Lifting Rotor Performance at High Advance Ratios." *Proceedings of the AHS Aeromechanics Specialists' Conference*, San Francisco, CA January 20–22, 2010.

[24] Quackenbush, T.R., Wachspress, D.A., McKillip, R. M. (Jr), and Sibilia, M. J., "Aerodynamic Studies of High Advance Ratio Rotor Systems." *Proceedings of the* 36th *European Rotorcraft Forum*, Paris, France, Sept 6–9, 2010.

[25] Jose, A.I., Ananthan, S., Baeder, J.D., "CFD/CSD Simulation of Baseline UH-60 and Swashplateless Rotors." *Proceedings of the AHS Aeromechanics Specialists' Conference*, San Francisco, CA January 2010.

[26] Peters D.A. and He C.J., "Comparison of Measured Induced Velocities with Results from a Closed-Form Finite State Wake Model in Forward Flight," *Proceedings of the* 45th *Annual Forum of the American Helicopter Society*, Boston, MA, May 1989.

[27] Chan, W., Meakin, R., and Potsdam, M., â"CHSSI Software for Geometrically Complex Unsteady Aerodynamic Applications," AIAA Paper 2001-0593, AIAA 39th Aerospace Sciences Meeting and Exhibit, Reno, NV, January 2001.

[28] Spalart, P. R., and Allmaras, S. R., "A One-Equation Turbulence Model for Aerodynamic Flows," AIAA 92-0439, 1991.